applied sciences

MDPI

Review

Biodegradable Contrast Agents for Photoacoustic Imaging

Su Woong Yoo [1], Doyoung Jung [2], Jung-Joon Min [1,3], Hyungwoo Kim [2,*] and Changho Lee [1,3,*]

1 Department of Nuclear Medicine, Chonnam National University Hwasun Hospital, 322, Seoyang-ro, Hwasun-eup, Hwasun-gun, Jeollanam-do 58128, Korea; yoosw.md@gmail.com (S.W.Y.); jjmin@jnu.ac.kr (J.-J.M.)

2 Alan G. MacDiarmid Energy Research Institute, School of Polymer Science and Engineering, Chonnam National University, 77 Yongbong-ro, Buk-gu, Gwangju 61186, Korea; 1993_jdy@naver.com

3 Department of Nuclear Medicine, Chonnam National University Medical School, 264, Seoyang-ro, Hwasun-eup, Hwasun-gun, Jeollanam-do 58128, Korea

* Correspondence: kimhw@jnu.ac.kr (H.K.); ch31037@jnu.ac.kr (C.L.); Tel.: +82-62-530-1775 (H.K.); +82-61-379-2885 (C.L.)

Received: 22 August 2018; Accepted: 3 September 2018; Published: 6 September 2018

Abstract: Over the past twenty years, photoacoustics—also called optoacoustics—have been widely investigated and, in particular, extensively applied in biomedical imaging as an emerging modality. Photoacoustic imaging (PAI) detects an ultrasound wave that is generated via photoexcitation and thermoelastic expansion by a short nanosecond laser pulse, which significantly reduces light and acoustic scattering, more than in other typical optical imaging and renders high-resolution tomographic images with preserving high absorption contrast with deep penetration depth. In addition, PAI provides anatomical and physiological parameters in non-invasive manner. Over the past two decades, this technique has been remarkably developed in the sense of instrumentation and contrast agent materials. In this review, we briefly introduce state-of-the-art multiscale imaging systems and summarize recent progress on exogenous bio-compatible and -degradable agents that address biomedical application and clinical practice.

Keywords: photoacoustic imaging; biodegradable; melanoidin; carbon dots; gold nanoparticles; polymers

1. Introduction

Photoacoustic imaging (PAI) is considered a promising volumetric imaging technique for biomedical applications based on hybrid contrast mechanism under a light illumination and emitted ultrasound capturing scheme which enables to provide spectroscopic optical contrast and ultrasonic high-resolution. Additionally, PAI can achieve deep tissue imaging (several centimeters) by overcoming the bottleneck of the typical optical penetration depth (theoretically ~1 mm) [1–8]. Furthermore, using the intrinsic optical absorption contrast between various components, including hemoglobin, melanoma, collagen and fat, PAI can visualize anatomical information such as vasculature distributions, melanin location, tendons and plaques, as well as physiological information such as the total amount of hemoglobin, oxygen saturation ratio, blood velocity and metabolic ratio [9–11]. In parallel, diverse PAI systems have been consistently developed with multiscale imaging ability [12]. Therefore, photoacoustic microscopy (PAM) achieves high spatial resolution with a focused excitation laser or a focused ultrasound transducer by scanning using a mechanical scanning stage or a high-speed optical scanner [13–15]. Also, photoacoustic computed tomography (PACT) delivers two- and

three-dimensional deep tissue PA images for various kinds of structural, functional and molecular imaging in macro- or micro-scale [16–21]. These benefits can be widely utilized in basic scientific research and clinical translation approaches in areas including dermatology, oncology, ophthalmology and neurology [10,11,22–25].

Although the intrinsic contrasts in biological tissue can provide multi-contrast PA images, the absorption peaks usually stay around the visible spectral range, which decreases the light penetration depth owing to strong light scattering and absorption. As a result, the intrinsic contrasts can only delineate the shallow-depth regions. Near-infrared light is suitable for deeper tissue imaging and exogenous contrast agents that absorb near-infrared light can significantly enhance the functionality of PAI [26]. In particular, high photoacoustic (PA) intensity signals are not obtained for transparent and colorless biological tissues such as the lymph nodes, bladder and intestines because they have relatively low absorption coefficients in the visible and near-infrared spectral regions. Thus, exogenous contrast agents with outstanding absorption capabilities in the near-infrared spectral region and the ability to target specific types of biological tissue can improve sensitivity, specificity and the contrast of PAI.

Diverse exogenous contrast agents, such as metallic agents (e.g., gold-, silver- and copper agents) [27–29], carbon-based agents (e.g., carbon nanotubes) [30], organic agents (e.g., porphyrin, lipid and polypyrrole agents) [31,32] and semi-conducting polymer agents [33] have been used as high-sensitivity PAI or theranostic contrast agents with superior absorption coefficients in the near-infrared spectral region. As one of the most widely used metallic agents, gold-based formulations, which produce a variety of gold structures, exhibit excellent PA signal enhancement [34–36]. However, their biocompatibility, biodegradability and renal clearance remain important issues for translation into real clinical applications. For instance, the clearance of gold nanoshells covered with polyethylene glycol (M_w = 5000) from the body is difficult [37]. The utilization of surfactants to synthesize gold nanorods may cause issues related to toxicity [38,39]. Moreover, carbon-based agents obtained by pyrolysis have been studied as novel molecular imaging agents. Unfortunately, pyrolysis processes cause considerable chemical and physical changes and unavoidably result in the formation of cytotoxic compounds [39–41].

To compensate for these problems, several biocompatible and biodegradable PA contrast agents have been reported recently. Melanoidin, which is composed of glucose and glycerin and nitrogen-doped carbon nanodots (N-CNDs), was introduced as a multifunctional PA contrast agent. They showed enough therapeutic effects (i.e., PAI and photothermal effects) with good biodegradability. Gold nanoparticles (AuNPs) and gold nanovesicles (GVs) also demonstrated biocompatibility while maintaining PAI performance. Furthermore, biodegradable polymers, including natural products and synthetic polymers, have been extensively used in PAI as: (i) signal transducers that generate PA signals; (ii) matrices that capture PA molecular probes; or (iii) dispersants/surfactants for photoactive species.

In this review, we provide an overview of recent progress in the development of biodegradable PA contrast agents from the perspective of instrumental design and materials science.

2. Melanoidin Nanoparticles as Biodegradable PA Agents

Melanoidin is commonly found in a variety of foods, such as coffee, bread and soy sauce. This heterogeneous nitrogen-containing pigment has a light absorption peak at 420 nm [42]. Lee et al. synthesized glucose-glycine melanoidin (GG-melanoidin) as a PA agent for imaging [43]. The Maillard reaction between glucose and glycine was used to synthesize GG-melanoidin at body temperature and pH. GG-melanoidin has high solubility in water and serum owing to its high content of hydroxyl and carboxyl groups (Figure 1A). The addition of Fe^{3+} produced a molecular complex (GG-melanoidin/Fe^{3+}) that showed an increased photothermal effect. The complex, which had a size of ca. 10 nm (Figure 1B), exhibited renal excretion without any significant abnormality (e.g., hair loss and necrosis) that was observed in the case of methylene blue (MB) dye. The measured PA amplitudes of GG-melanoidin (2.5 $\pm$ 0.2) and GG-melanoidin/Fe^{3+} (2.7 $\pm$ 0.2) were higher than those of gold

nanorods (0.4 ± 0.03) and MB (1.2 ± 0.1) at the same optical density (Figure 1C). Owing to its high PA signal, three-dimensional PA images (Figure 1D) and depth-resolved two-dimensional PA images (Figure 1E) clearly showed the location of sentinel lymph nodes (SLNs) filled with melanoidin. Melanoidin initially accumulated in the SLNs and then slowly escaped because of circulation activity in the lymph nodes and the lymphatic vessels. Therefore, this biodegradable melanoidin is a promising theranostic agent for biomedical application.

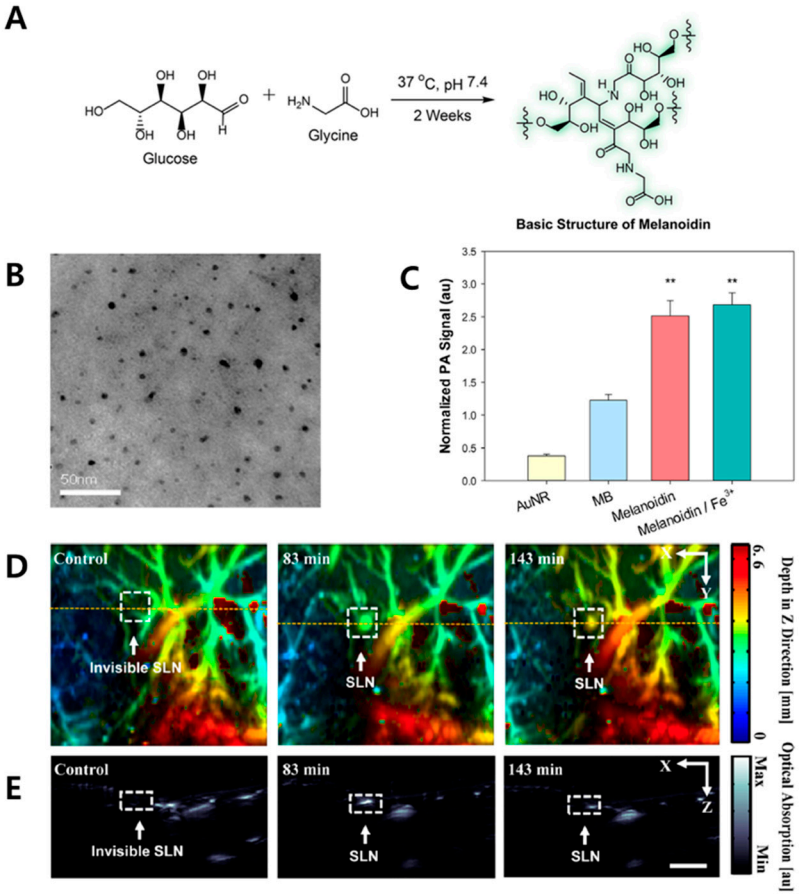

Figure 1. Melanoidin nanoparticles. (**A**) Schematic of GG-melanoidin. (**B**) Transmission electron microscopy (TEM) image of GG-melanoidin/Fe^{3+}. (**C**) Comparison of the PA signals of GG-melanoidin, GG-melanoidin/Fe^{3+}, gold nanorods (AuNR) and methylene blue (MB) under irradiation at 680 nm. (**D**) Three-dimensional PA images and (**E**) depth-resolved two-dimensional PA images of sentinel lymph nodes. Reproduced with permission from [43]. Copyright American Chemical Society, 2016.

3. Nitrogen-Doped Carbon Nanodots as Biodegradable PA Agents

Carbon-based nanoparticles have been investigated as therapeutic agents for PAI and photothermal therapy owing to their strong photoabsorbtion ability, biocompatibility, water solubility and photostability [44–47]. However, biodegradability is the main challenge of these materials. Lee et al. synthesized nitrogen-doped carbon nanodots (N-CNDs) to overcome this issue [48]. N-CNDs were produced by the solvothermal carbonization of citric acid in nitric acid (Figure 2A). First, a heated mixture of citric acid and nitric acid formed polymer-like intermediates by dehydration. Then, the intermediates underwent carbonization to generate carbogenic cores. Simultaneously, oleylamine was implanted on the surface of the core to inhibit undesired intergranular aggregation during the carbonization process. Finally, oleylamine was replaced with ethanolamine to improve the water solubility. The N-CNDs were determined to have a size of approximately 3 nm (Figure 2B). The amplitude of the measured PA signals of N-CNDs (2.2 ± 0.2) was better than those of gold nanorods (1.0 ± 0.1) and MB (1.3 ± 0.1) (Figure 2C). As photothermal agents,

aqueous solutions of N-CNDs showed temperature changes when irradiated with an 808 nm laser (Figure 2D). Time-course PA images of SLNs in a rat model showed that the signal increased 30 min after intradermal injection of the N-CNDs (Figure 2E). Subsequently, the PA signal of the SLNs gradually decreased until 180 min (Figure 2F).

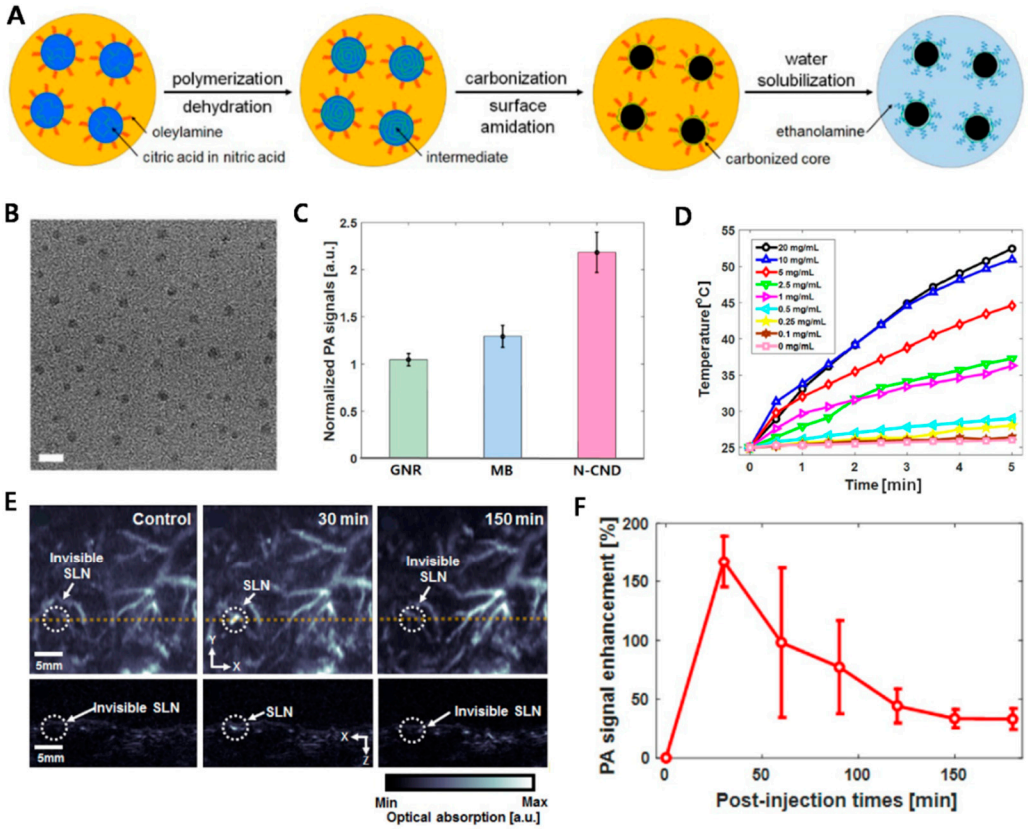

Figure 2. Nitrogen-doped carbon nanodots (N-CNDs) as theranostic agents. (**A**) Synthesis of N-CNDs. (**B**) TEM image of N-CNDs (scale bar = 5 nm). (**C**) Comparison of the PA signals of gold nanorods (GNR), methylene blue (MB) and N-CNDs. (**D**) Temperature changes of different concentrations of N-CNDs under irradiation at 808 nm. (**E**) Three-dimensional PA images (upper row) and depth-resolved two-dimensional PA images (lower row) in sentinel lymph nodes (SLNs) before (control), 30 min and 150 min after the injection of N-CNDs. (**F**) PA signal changes in the SLN area over time. Reproduced with permission from [48]. Copyright Ivyspring International Publisher, 2016.

The PA signal of the bladder increased 100 min after the time of injection and an enhanced signal was observed until 450 min, indicating that renal clearance occurred in the rat body. Therefore, these biodegradable carbon nanodots are a promising PA contrast agent and photothermal therapeutic agent.

4. Gold Nanoparticles as Biodegradable PA Agents

The characteristics of gold nanoparticles (AuNPs) are inert and biocompatible and can be varied through ligand attachment and shape modification [49–51]. Although various AuNPs has been demonstrated as molecular PAI contrast agents [52–54], there are no FDA-approved AuNPs owing to concerns related to hepatic retention. To achieve efficient renal clearance, the particles should be smaller than approximately 6 nm [55]. Therefore, several attempts have been made to make biodegradable AuNPs platforms that can be degraded under specific conditions.

4.1. Polymer-Stabilized AuNP Clusters for PAI

Polymer-stabilized AuNPs have been applied to PAI. Tam et al. assembled sub-5 nm AuNPs with the triblock copolymer of polylactic acid and polyethylene glycol, PLA(2K)-*b*-PEG(10K)-*b*-PLA(2K) [56]. The primary AuNPs were aggregated in the presence of the polymer (Figure 3A). The average diameter of the primary AuNPs was 4.1 ± 0.8 nm (Figure 3B). Changing the polymer-to-AuNP ratio, the AuNP concentration and the surface ligands on the primary AuNPs made it possible to control the size of the clustered AuNPs. Deaggregation of the AuNP clusters occurred within live cells (Figure 3C). The 40-nm sized AuNP clusters, which showed a higher PA signal intensity than gold nanorods (Figure 3D), are another promising PA contrast agent [36].

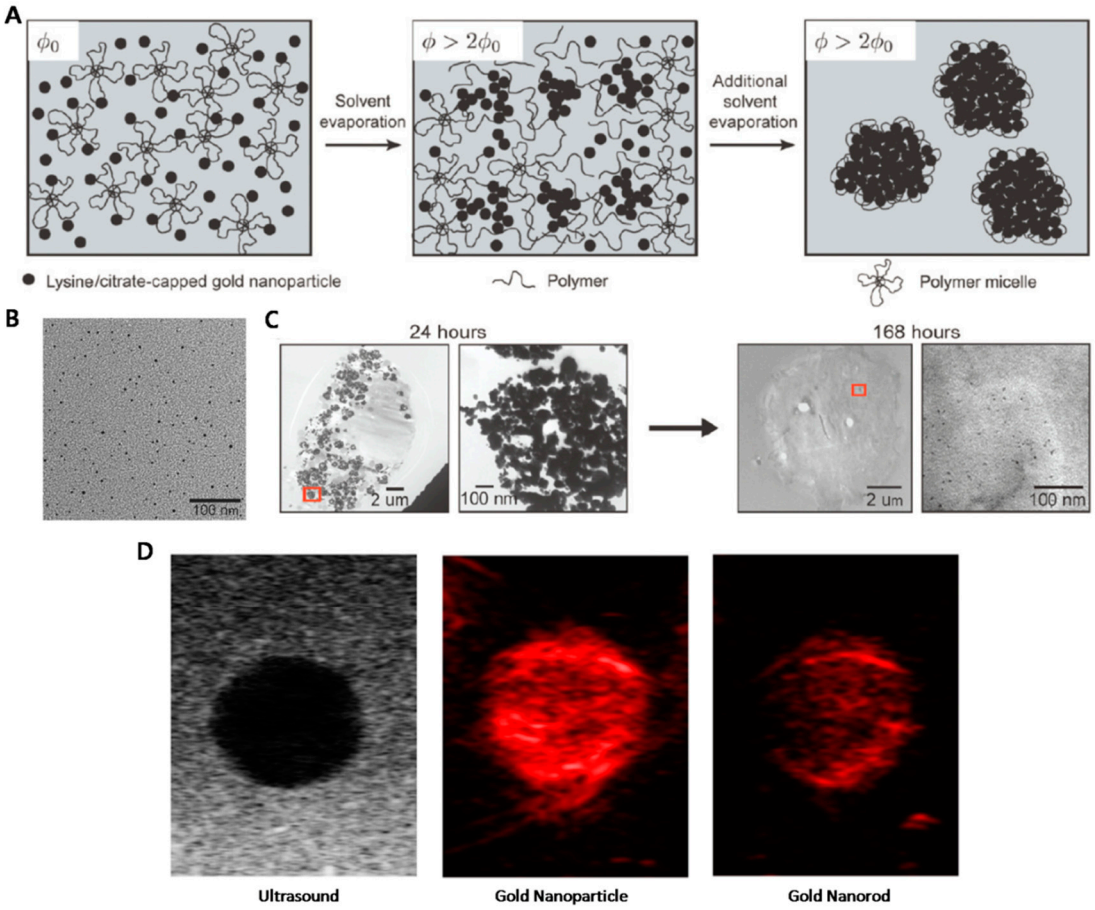

Figure 3. Polymer-stabilized gold nanoparticle (AuNP) clusters. (**A**) The formation process for AuNP clusters. Aggregation of the AuNPs and the polymer increased the volume fraction of the particles (ϕ). (**B**) Electron microscope image of 4 nm sized primary AuNPs. (**C**) Low- and high-magnification images of biodegradation of the AuNP clusters in live cells at 24 and 168 h. The red squares in the low-magnification images correspond to the areas shown in the high-magnification images. (**D**) An ultrasound image of the hypoechoic inclusion with hyperechoic background (left). Photoacoustic images of the phantom with inclusions containing AuNPs (middle) or gold nanorods (right). Reproduced with permission from [36,56]. Copyright, American Chemical Society (2010) and Optical Society of America (2012).

4.2. Biodegradable Gold Nanovesicles as Theranostic Agents

In addition to PAI, AuNPs can simultaneously be used as photothermal therapy agents. Huang et al. produced biodegradable gold nanovesicles (BGVs) consisting of poly(ethylene glycol)-*b*-poly(ε-caprolactone) (PEG-*b*-PCL)-tethered AuNPs [34]. Each BGV had a single layer of AuNPs with a hollow interior cavity (Figure 4A). The average PA signal intensity of the BGVs

was approximately ten times higher than the background and two times higher than that of GVs, which composed of nonbiodegradable PEG-*b*-polystyrene polymer-tethered AuNPs (Figure 4B). The intense PA signal was monitored in the tumoral area after intratumoral injection of the BGVs in a mouse model with an MDA-MB-435 tumor (Figure 4C). Owing to strong near-infrared absorption properties, the BGVs showed a higher photothermal conversion efficiency (37%) than GVs (18%), gold nanorods (22%) and gold nanoshells (13%).

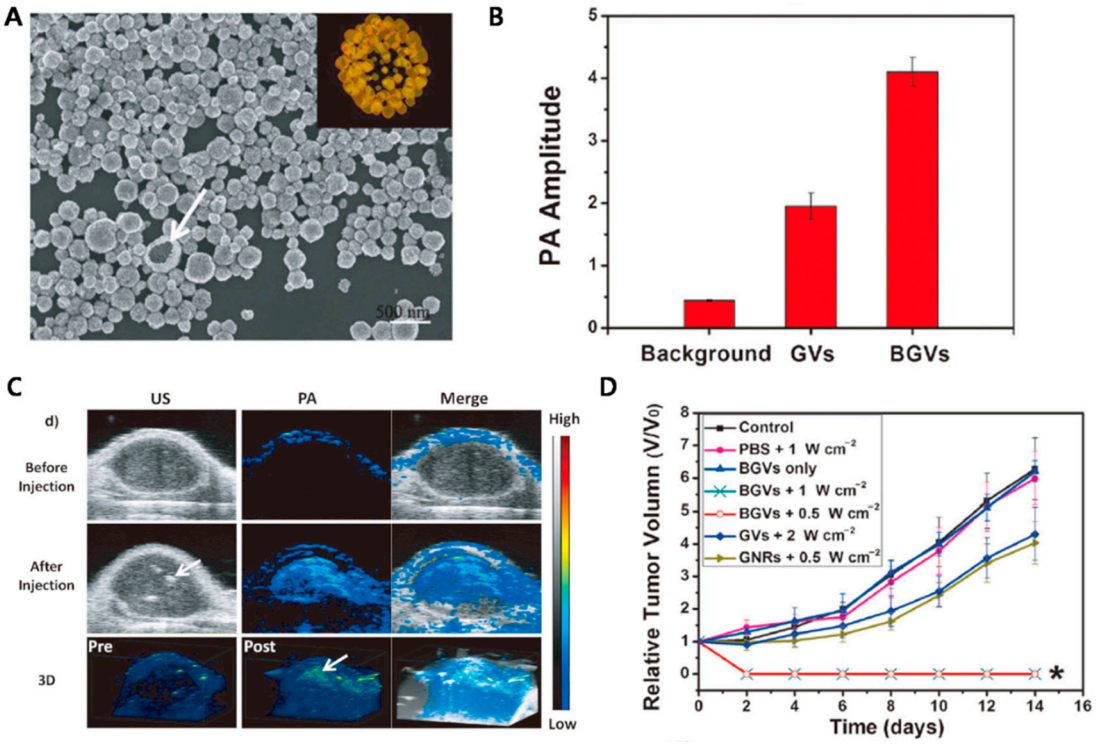

Figure 4. Biodegradable gold vesicles (BGVs). (**A**) Scanning electron microscopy image of BGVs (inset: 3D electron density map of a broken BGV). (**B**) PA signal intensities in tumor tissue after intratumoral injection of gold vesicles (GVs) and BGVs. (**C**) In vivo depth-resolved two-dimensional ultrasound, PAI and volumetric PAI and ultrasound images of tumor tissue before and after injection of BGVs. (**D**) Tumor growth in each group of MDA-MB-435 tumor-bearing mice. Reproduced with permission from [34]. Copyright John Wiley and Sons, 2013.

The BGVs gradually began to break down when the system temperature exceeded 70 °C. Because PCL has a melting point of approximately 60 °C, most of the BGVs were degraded after 10 min. Under irradiation with an 808 nm laser, tumors injected with the BGVs showed retarded growth and tumor regression (Figure 4D). Therefore, these BGVs are promising multifunctional theranostic platforms for PAI and photothermal therapeutic applications. More recent works on BGVs used smaller primary AuNPs to increase the biocompatibility and enhance the renal excretion of the degraded AuNPs [35].

5. Polymeric Materials as Biodegradable PA Agents

Benefiting from the development of polymer science and nanotechnology, polymeric materials have attracted great attention as a new class of PA agents that offers considerable structural diversity and designed material properties via chemical functionalization [57–64]. Notably, polymer nanoparticles have been successfully demonstrated as molecular imaging agents [65]. Such nanoparticles principally consist of π-conjugated polymer cores and hydrophilic polymer shells, which are generally formed via nanoprecipitation or nanoemulsion techniques. Therefore, the photophysical properties of a semi-conducting polymer can be translated into detectable ultrasonic signals in response to laser

pulses, while a peripheral surfactant polymer stabilizes the overall structure under physiological conditions. Seminal review papers have covered semi-conducting-polymer-based PA agents [66,67]. In contrast, this section focuses on polymeric materials for biodegradable contrast agents. For this purpose, the agents are expected to be biocompatible, or at least amphiphilic, possess cleavable bonds, or exhibit the desired optical properties [68–70]. As an example, owing to their intrinsic properties, natural polymeric materials such as polysaccharides, phospholipids and deoxyribonucleic acid (DNA) can be used as biodegradable agents (Figure 5). In addition, conventional hydrophilic polymers play a key role as an essential component for the biocompatibility of organic nanostructures including particles, hydrogels, micelles, vesicles and polymersomes [68,71–75]. Theses polymers have been incorporated into contrast agents through controlled polymerization, copolymerization, or postpolymerization modification (Figure 6). More interestingly, functional polymers that have chemically removable groups (e.g., labile groups, stimuli-responsive groups, or self-immolative groups) have shown biodegradability when exposed to bio-related signals such as pH, enzymes, temperature and biogenic chemicals.

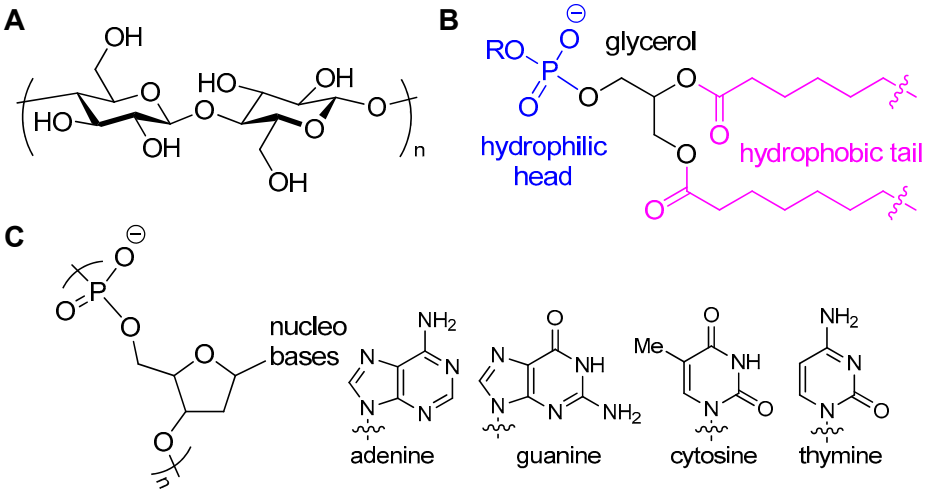

Figure 5. Chemical structures of (**A**) cellulose, (**B**) phospholipid and (**C**) deoxyribonucleic acid (DNA).

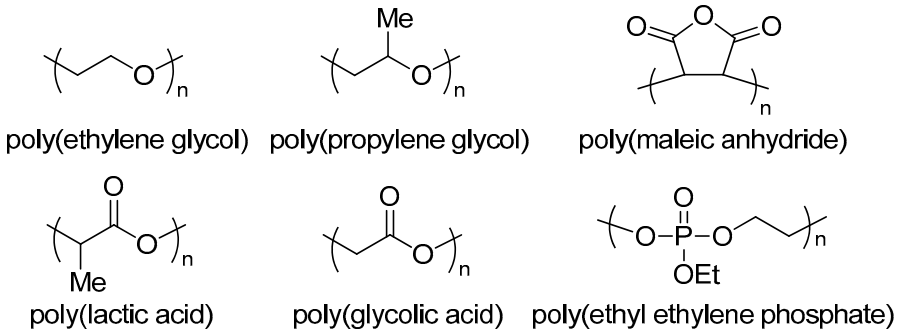

Figure 6. Typical synthetic polymeric components incorporated into various nanostructures for PA agents via controlled polymerization, copolymerization, or postpolymerization modification.

5.1. Natural Polymers as PA Agents

The major advantages of using natural products include not only good dispersibility under physiological conditions, but also the availability of metabolic clearance pathways, which prevents nonspecific, long-term accumulation in biological systems. Cellulose, a renewable biomass, has been used as a biodegradable contrast agent, as demonstrated by the Gambhir group [76]. Highly crystalline cellulose nanocrystals were prepared by acid treatment. Rayleigh scattering from the material was observed over a wide spectral range, enabling PAI when excited at 700 nm. The resulting PA signal was comparable to or even better than that of gold nanorods (GNRs) (Figure 7). The crystals were

degradable in the presence of cellulase, an enzyme capable of decomposing polysaccharides such as cellulose which humans lack. However, it was claimed that the agent can be used as a smart probe triggered by the external enzyme stimulus, as revealed by detecting the concentration of glucose (the repeating unit of cellulose) after decomposition and by transmission electron microscopy.

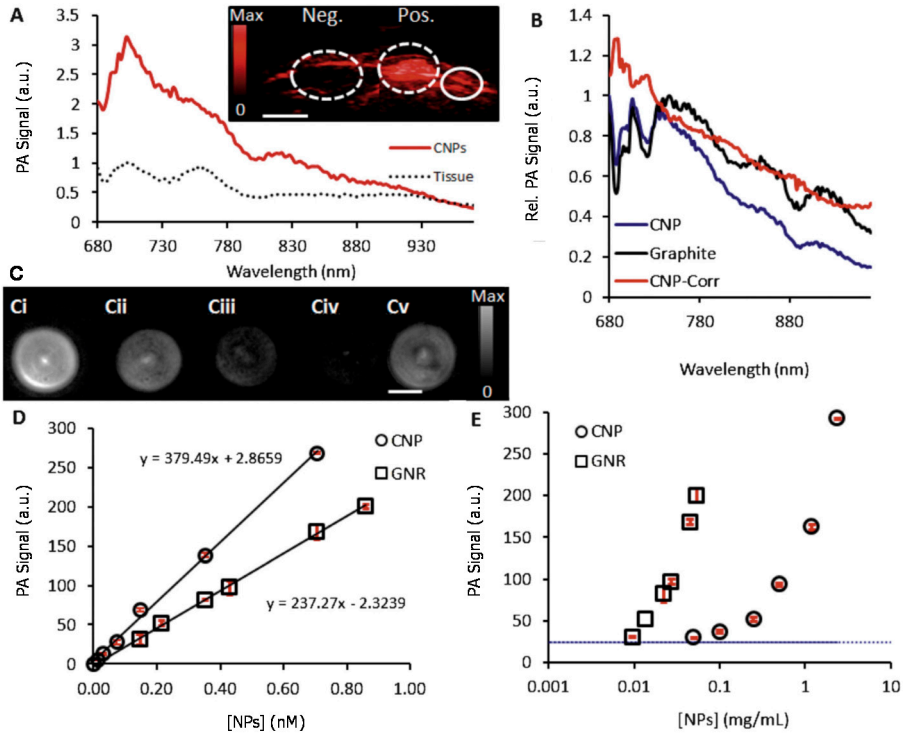

Figure 7. PA signaling of cellulose nanoparticles (CNPs). (**A**) Spectral imaging of CNPs, showing a maximum absorbance peak at 700 nm, which was used for all subsequent imaging experiments (red solid curve). The background PA spectrum of normal tissue is also shown for reference (black dots). The inset shows a PA image of a subcutaneously implanted bolus of CNPs at 0.5 mg·mL^{-1} ("Pos.") and a matrigel only implant ("Neg."). The solid circle highlights a normal region used to create the tissue-only spectrum. The scale bar in the inset is 3 mm. (**B**) Normalized PA data for CNPs and a "flat" graphite absorber, illustrating the change in laser power as a function of wavelength. (**C**) Representative PA images of a phantom scanned with a tomographic imaging system. Ci–Civ are CNPs. Ci: 0.70 nM, Cii: 0.35 nM; Ciii: 0.15 nM; Civ: 0.07 nM. Cv is 0.70 nM GNRs. Scale bar in C is 4 mm. PA data for CNPs and GNRs collected using the tomographic scanner for both CNPs and GNRs with 700 nm incident radiation using either molar (**D**) or mass units (**E**). Error bars in C are plotted in red and represent the standard deviation of 3 replicate samples and are <10% RSD. Reprinted with permission from [76]. Copyright Elsevier, 2014.

5.2. Biodegradable Polymers as PA Agents

Conventional biodegradable synthetic polymers have been extensively applied as contrast agents for PAI, as mentioned above. As a representative example, poly(lactic-*co*-glycolic acid) (PLGA) can be used for biodegradable agents. The polymer is typically obtained from cyclic monomers of lactic acid and glycolic acid through statistical copolymerization or block copolymerization (Figure 8A). Because of the ester linkages in the backbone, PLGA is subject to hydrolysis under aqueous conditions. Furthermore, the composition ratio between lactic acid and glycolic acid determines the rate of hydrolysis. The higher the content of glycolide repeating units, the faster the polymer hydrolyzes. In contrast, the incorporation of lactide units tends to retard the degradation. Wang et al. used PLGA to fabricate a biodegradable nanoparticle agent through the double emulsion method [77]. Herein, PLGA positioned in a polymer shell and imparted biodegradability as well as sufficient mechanical properties to the nanoparticles. Therefore, the resulting hierarchical PLGA-based agent

was multimodal: (i) the agent was able to generate PA signals when stimulated by a laser pulse owing to AuNPs incorporated in the core, (ii) further incorporation of a dye in the core enabled fluorescent imaging and (iii) the agent showed potential for delivering paclitaxel, a cancer therapeutic drug, as demonstrated by in vitro experiments. Thus, theragnosis—a combined concept of remedial therapy and diagnostic imaging—was achieved.

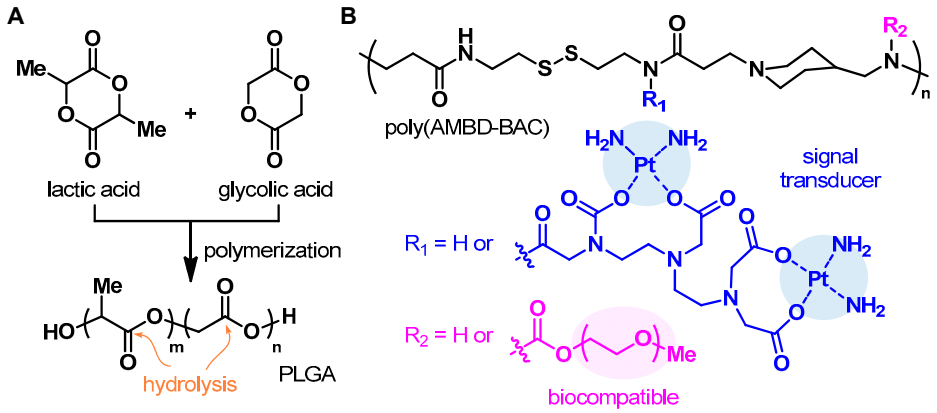

Figure 8. (**A**) Synthetic procedure for poly(lactide-*co*-glycolide) (PLGA) using cyclic dimers of lactic acid and glycolic acid. The resulting copolymer has ester linkages that provide a hydrolytic response in the backbone. (**B**) Chemical structure of poly(aminomethylpiperidine-bis(acryloyl)cystamine) (poly(AMBD-BAC)) containing Pt(II)-based signal transducers and poly(ethylene glycol) side chains. The chemical structures of the side chains are shown below the polymer structure.

In another example, a synthetic block copolymer that contains Pt(II) complexes was used [78]. In this work, an organic–inorganic hybrid contrast agent was designed using functional polymers. First, the polymerization of equimolar amounts of 4-aminomethyl piperidine (AMPD) and equimolar *N*,*N*′-bis(acryloyl)cystamine (BAC) via a Michael addition reaction afforded the poly(AMBD-BAC) backbone. The disulfide bond in BAC provided redox-responsive behavior and was cleaved when exposed to glutathione (GSH). Postpolymerization modification introduced poly(ethylene glycol) moieties into the backbone, which facilitated drug delivery and reduced nonspecific adsorption during circulation in physiological environments. Furthermore, diethylenetriaminepentaacetic acid (DTPA) and Cisplatin were added sequentially to form Pt(II) complexes that generated PA signals (Figure 8B). The functional polymers were developed into nanoparticles under aqueous conditions and the resulting particles allowed in vivo imaging of rat cerebral vasculature, taking advantage of the PA signal. Cytotoxicity tests further confirmed that the polymeric material was biocompatible.

5.3. Functional Polymers as PA Agents

Cleavable chemical groups give rise to biodegradability in polymeric contrast agents. Recently, Lyu et al. have designed functional nanoparticle agents for PAI (Figure 9) [79]. The semi-conducting polymer core of these particles generated not only PA signals but also heat for photothermal therapy. The core polymer was further tethered with poly(ethylene glycol) methyl ether-*b*-poly(lactide-*co*-glycolide) (PLGA-*co*-PEG), which endowed biocompatibility and water dispersibility (Figure 9C). In particular, the semiconducting polymer, DPPV (Figure 9A), had vinylene groups in the backbone. Thus, the whole chain was fully π-conjugated but the oxidizable nature of the vinylene group allowed degradation of the chain, which is in contrast to DPPT (Figure 9B). As a result, the particles, SPNV (DPPV-based polymer nanoparticle) and SPNT (DPPT-based polymer nanoparticle), showed comparable PAI and photothermal therapy simultaneously (Figure 9D–I) but SPNV was only degraded biologically to monomeric species in the presence of a peroxidase enzyme (myeloperoxidase) reducing the signal. Notwithstanding, the examples of well-designed, biodegradable, functional polymers for PAI are still rare as far as we know. The use of other chemistry, such as continuous

depolymerization [80–82] and dynamic physicochemical bonds or the formation of reversible and hierarchical structures of polymeric materials [83–86], would further provide new, biocompatible, degradation pathways of polymer structures without losing PA properties.

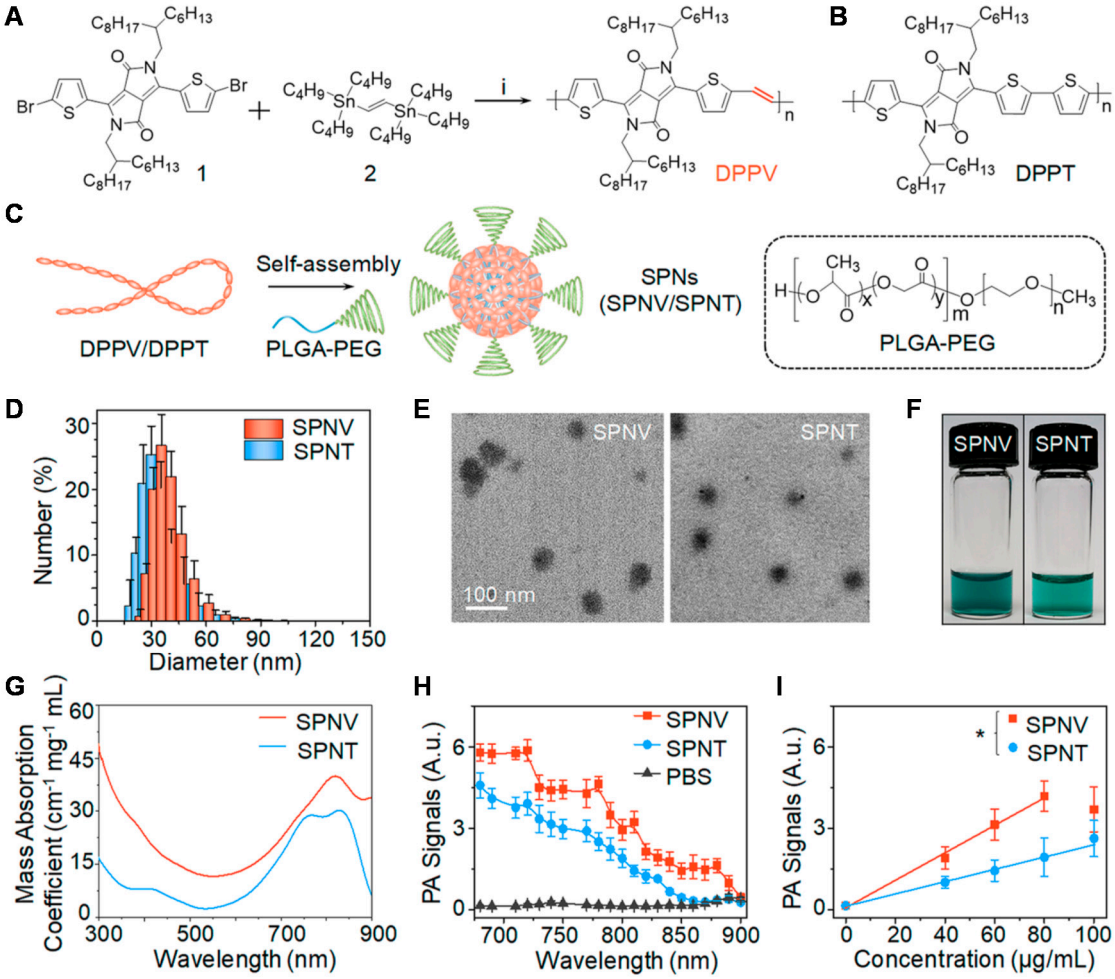

Figure 9. Synthesis and characterization of semi-conducting polymer nanoparticles (SPNs). (**A**) Synthetic route for DPPV. (i) $Pd_2(dba)_3$ and tri(*o*-tolyl) phosphine, toluene, 100 °C, 24 h. (**B**) Chemical structure of DPPT. (**C**) Chemical structure of PLGA-*co*-PEG and schematic illustration of the preparation of SPNs. (**D**) DLS profiles, (**E**) transmission electron microscopy images, (**F**) photographs of solutions and (**G**) absorption spectra of SPNV (DPPV-based SPN) and SPNT (DPPT-based SPN). (**H**) PA spectra of SPNV, SPNT and PBS. (**I**) PA intensities at 810 nm as a function of the concentrations (0–100 μg·mL^{-1}) of SPNV and SPNT (R^2 = 0.992 and 0.995 for SPNV and SPNT, respectively). The SPN solutions were prepared in PBS buffer (pH 7.4). The 60 μg·mL^{-1} solutions were used for photography and the PA spectral measurements. A single laser pulse (energy, 100 mJ pulse^{-1}; duration, 5 ns; pulse repetition rate, 10 Hz) was used for the PA intensity measurements. The error bars are based on the standard deviations of three parallel samples. * Statistically significant differences in the PA intensities of SPNV and SPNT in the concentration range from 0 to 80 μg·mL^{-1} ($p < 0.01$, $n = 3$). Reprinted with permission from [79]. Copyright American Chemical Society, 2018.

6. Conclusions

PAI is a new class of preclinical and clinical biomedical imaging techniques owing to its unique ability to generate multicontrast images, as well as its relatively deep penetration depth and high spatial resolution. Various types of contrast agents have been investigated to obtain significant contrast and sensitivity in invisible biological tissues and the deep biological tissue region. Although many PA contrast agents demonstrated their ability at the preclinical level, clinical applications have been

limited by biodegradability issues. Recently, several studies have been devoted to the development of biocompatible and biodegradable PA materials, including melanoidin, N-CNDs, polymer-stabilized AuNP clusters, GVs and polymeric agents. However, for clinical and commercial applications, focused systemic investigations are necessary to (i) enhance renal clearance efficiency, (ii) achieve high photostability, (iii) decrease phototoxicity and (iv) develop large-scale production methods. In addition, to demonstrate the biodistribution and pharmacokinetics of nanoparticles for clinical translation, rigorous experiments and analyses should be conducted with careful consideration of the chemical composition, structure, size and surface modification of the contrast agents. Moreover, as contrast agent studies have been conducted primarily in the field of cancer imaging and therapy, there is a need to expand the research to identify the potential of this technique in a variety of areas such as heart, brain and neurological diseases.

Author Contributions: S.W.Y. and J.-J.M. contributed to writing Sections 2–4; D.J. conducted a literature survey; C.L. and H.K. organized the structure of the review article; all authors participated in writing the paper.

Funding: This work was supported by the National Research Foundation of Korea (NRF) grant funded by the Korea government (MSIT, Ministry of Science and ICT) (No. 2017R1C1B5017785) and Chonnam National University (No. 2017-1779) to H.K. and NRF grant funded by the Korea government (MSIT) (No. 2017R1C1B5018181) and the Pioneer Research Center Program through the NRF of Korea funded by the Ministry of Science, ICT & Future Planning (No. 2015M3C1A3056407) to C.L.

Conflicts of Interest: The authors declare no conflict of interest.

References

1. Bell, A.G. The photophone. *Science* **1880**, *1*, 130–134. [CrossRef] [PubMed]
2. Cai, X.; Kim, C.; Pramanik, M.; Wang, L.V. Photoacoustic tomography of foreign bodies in soft biological tissue. *J. Biomed. Opt.* **2011**, *16*, 046017. [CrossRef] [PubMed]
3. Zhang, Y.; Jeon, M.; Rich, L.J.; Hong, H.; Geng, J.; Zhang, Y.; Shi, S.; Barnhart, T.E.; Alexandridis, P.; Huizinga, J.D.; et al. Non-invasive multimodal functional imaging of the intestine with frozen micellar naphthalocyanines. *Nat. Nanotechnol.* **2014**, *9*, 631–638. [CrossRef] [PubMed]
4. Lee, C.; Han, S.; Kim, S.; Jeon, M.; Jeon, M.Y.; Kim, C.; Kim, J. Combined photoacoustic and optical coherence tomography using a single near-infrared supercontinuum laser source. *Appl. Opt.* **2013**, *52*, 1824–1828. [CrossRef] [PubMed]
5. Kim, J.Y.; Lee, C.; Park, K.; Han, S.; Kim, C. High-speed and high-snr photoacoustic microscopy based on a galvanometer mirror in non-conducting liquid. *Sci. Rep.* **2016**, *6*, 34803. [CrossRef] [PubMed]
6. Park, K.; Kim, J.Y.; Lee, C.; Jeon, S.; Lim, G.; Kim, C. Handheld photoacoustic microscopy probe. *Sci. Rep.* **2017**, *7*, 13359. [CrossRef] [PubMed]
7. Lee, D.; Lee, C.; Kim, S.; Zhou, Q.; Kim, J.; Kim, C. In vivo near infrared virtual intraoperative surgical photoacoustic optical coherence tomography. *Sci. Rep.* **2016**, *6*, 35176. [CrossRef] [PubMed]
8. Lee, C.; Jeon, M.; Jeon, M.Y.; Kim, J.; Kim, C. In vitro photoacoustic measurement of hemoglobin oxygen saturation using a single pulsed broadband supercontinuum laser source. *Appl. Opt.* **2014**, *53*, 3884–3889. [CrossRef] [PubMed]
9. Hu, S.; Maslov, K.; Wang, L.V. Second-generation optical-resolution photoacoustic microscopy with improved sensitivity and speed. *Opt. Lett.* **2011**, *36*, 1134–1136. [CrossRef] [PubMed]
10. Wang, Y.; Maslov, K.; Zhang, Y.; Hu, S.; Yang, L.; Xia, Y.; Liu, J.; Wang, L.V. Fiber-laser-based photoacoustic microscopy and melanoma cell detection. *J. Biomed. Opt.* **2011**, *16*, 011014. [CrossRef] [PubMed]
11. Yao, J.; Maslov, K.I.; Zhang, Y.; Xia, Y.; Wang, L.V. Label-free oxygen-metabolic photoacoustic microscopy in vivo. *J. Biomed. Opt.* **2011**, *16*, 076003. [CrossRef] [PubMed]
12. Zhang, Y.; Hong, H.; Cai, W. Photoacoustic imaging. *Cold Spring Harb. Protoc.* **2011**, *2011*, 1015–1025. [CrossRef] [PubMed]
13. Beard, P. Biomedical photoacoustic imaging. *Interface Focus* **2011**, *1*, 602–631. [CrossRef] [PubMed]
14. Park, S.; Lee, C.; Kim, J.; Kim, C. Acoustic resolution photoacoustic microscopy. *Biomed. Eng. Lett.* **2014**, *4*, 213–222. [CrossRef]

15. Jeon, M.; Kim, J.; Kim, C. Multiplane spectroscopic whole-body photoacoustic imaging of small animals in vivo. *Med. Biol. Eng. Comput.* **2016**, *54*, 283–294. [CrossRef] [PubMed]
16. Su, J.L.; Wang, B.; Wilson, K.E.; Bayer, C.L.; Chen, Y.S.; Kim, S.; Homan, K.A.; Emelianov, S.Y. Advances in clinical and biomedical applications of photoacoustic imaging. *Expert Opin. Med. Diagn.* **2010**, *4*, 497–510. [CrossRef] [PubMed]
17. Xu, M.H.; Wang, L.H.V. Photoacoustic imaging in biomedicine. *Rev. Sci. Instrum.* **2006**, *77*, 041101. [CrossRef]
18. Xia, J.; Yao, J.; Wang, L.V. Photoacoustic tomography: Principles and advances. *Electromagn. Waves* **2014**, *147*, 1–22. [CrossRef]
19. Nasiriavanaki, M.; Xia, J.; Wan, H.; Bauer, A.Q.; Culver, J.P.; Wang, L.V. High-resolution photoacoustic tomography of resting-state functional connectivity in the mouse brain. *Proc. Natl. Acad. Sci. USA* **2014**, *111*, 21–26. [CrossRef] [PubMed]
20. Wang, X.; Ku, G.; Wegiel, M.A.; Bornhop, D.J.; Stoica, G.; Wang, L.V. Noninvasive photoacoustic angiography of animal brains in vivo with near-infrared light and an optical contrast agent. *Opt. Lett.* **2004**, *29*, 730–732. [CrossRef] [PubMed]
21. Yao, J.; Kaberniuk, A.A.; Li, L.; Shcherbakova, D.M.; Zhang, R.; Wang, L.; Li, G.; Verkhusha, V.V.; Wang, L.V. Multiscale photoacoustic tomography using reversibly switchable bacterial phytochrome as a near-infrared photochromic probe. *Nat. Methods* **2016**, *13*, 67–73. [CrossRef] [PubMed]
22. Zhou, Y.; Xing, W.; Maslov, K.I.; Cornelius, L.A.; Wang, L.V. Handheld photoacoustic microscopy to detect melanoma depth in vivo. *Opt. Lett.* **2014**, *39*, 4731–4734. [CrossRef] [PubMed]
23. Zhang, C.; Cheng, Y.J.; Chen, J.; Wickline, S.; Wang, L.V. Label-free photoacoustic microscopy of myocardial sheet architecture. *J. Biomed. Opt.* **2012**, *17*, 060506. [CrossRef] [PubMed]
24. Hu, S.; Wang, L.V. Neurovascular photoacoustic tomography. *Front. Neuroenergetics* **2010**, *2*, 10. [CrossRef] [PubMed]
25. Jiao, S.; Jiang, M.; Hu, J.; Fawzi, A.; Zhou, Q.; Shung, K.K.; Puliafito, C.A.; Zhang, H.F. Photoacoustic ophthalmoscopy for in vivo retinal imaging. *Opt. Express* **2010**, *18*, 3967–3972. [CrossRef] [PubMed]
26. Kim, C.; Favazza, C.; Wang, L.V. In vivo photoacoustic tomography of chemicals: High-resolution functional and molecular optical imaging at new depths. *Chem. Rev.* **2010**, *110*, 2756–2782. [CrossRef] [PubMed]
27. Chen, J.; Yang, M.; Zhang, Q.; Cho, E.C.; Cobley, C.M.; Kim, C.; Glaus, C.; Wang, L.V.; Welch, M.J.; Xia, Y. Gold nanocages: A novel class of multifunctional nanomaterials for theranostic applications. *Adv. Funct. Mater.* **2010**, *20*, 3684–3694. [CrossRef]
28. Homan, K.A.; Souza, M.; Truby, R.; Luke, G.P.; Green, C.; Vreeland, E.; Emelianov, S. Silver nanoplate contrast agents for in vivo molecular photoacoustic imaging. *ACS Nano* **2012**, *6*, 641–650. [CrossRef] [PubMed]
29. Liu, X.; Lee, C.; Law, W.C.; Zhu, D.; Liu, M.; Jeon, M.; Kim, J.; Prasad, P.N.; Kim, C.; Swihart, M.T. Au-$Cu_{(2-x)}$Se heterodimer nanoparticles with broad localized surface plasmon resonance as contrast agents for deep tissue imaging. *Nano Lett.* **2013**, *13*, 4333–4339. [CrossRef] [PubMed]
30. De la Zerda, A.; Zavaleta, C.; Keren, S.; Vaithilingam, S.; Bodapati, S.; Liu, Z.; Levi, J.; Smith, B.R.; Ma, T.J.; Oralkan, O.; et al. Carbon nanotubes as photoacoustic molecular imaging agents in living mice. *Nat. Nanotechnol.* **2008**, *3*, 557–562. [CrossRef] [PubMed]
31. Lovell, J.F.; Jin, C.S.; Huynh, E.; Jin, H.; Kim, C.; Rubinstein, J.L.; Chan, W.C.; Cao, W.; Wang, L.V.; Zheng, G. Porphysome nanovesicles generated by porphyrin bilayers for use as multimodal biophotonic contrast agents. *Nat. Mater.* **2011**, *10*, 324–332. [CrossRef] [PubMed]
32. Zha, Z.; Deng, Z.; Li, Y.; Li, C.; Wang, J.; Wang, S.; Qu, E.; Dai, Z. Biocompatible polypyrrole nanoparticles as a novel organic photoacoustic contrast agent for deep tissue imaging. *Nanoscale* **2013**, *5*, 4462–4467. [CrossRef] [PubMed]
33. Pu, K.; Shuhendler, A.J.; Jokerst, J.V.; Mei, J.; Gambhir, S.S.; Bao, Z.; Rao, J. Semiconducting polymer nanoparticles as photoacoustic molecular imaging probes in living mice. *Nat. Nanotechnol.* **2014**, *9*, 233–239. [CrossRef] [PubMed]
34. Huang, P.; Lin, J.; Li, W.; Rong, P.; Wang, Z.; Wang, S.; Wang, X.; Sun, X.; Aronova, M.; Niu, G.; et al. Biodegradable gold nanovesicles with an ultrastrong plasmonic coupling effect for photoacoustic imaging and photothermal therapy. *Angew. Chem. Int. Ed.* **2013**, *52*, 13958–13964. [CrossRef] [PubMed]
35. Cheheltani, R.; Ezzibdeh, R.M.; Chhour, P.; Pulaparthi, K.; Kim, J.; Jurcova, M.; Hsu, J.C.; Blundell, C.; Litt, H.I.; Ferrari, V.A.; et al. Tunable, biodegradable gold nanoparticles as contrast agents for computed tomography and photoacoustic imaging. *Biomaterials* **2016**, *102*, 87–97. [CrossRef] [PubMed]

36. Yoon, S.J.; Murthy, A.; Johnston, K.P.; Sokolov, K.V.; Emelianov, S.Y. Thermal stability of biodegradable plasmonic nanoclusters in photoacoustic imaging. *Opt. Express* **2012**, *20*, 29479–29487. [CrossRef] [PubMed]
37. Gad, S.C.; Sharp, K.L.; Montgomery, C.; Payne, J.D.; Goodrich, G.P. Evaluation of the toxicity of intravenous delivery of auroshell particles (gold-silica nanoshells). *Int. J. Toxicol.* **2012**, *31*, 584–594. [CrossRef] [PubMed]
38. Huang, P.; Bao, L.; Zhang, C.; Lin, J.; Luo, T.; Yang, D.; He, M.; Li, Z.; Gao, G.; Gao, B.; et al. Folic acid-conjugated silica-modified gold nanorods for x-ray/ct imaging-guided dual-mode radiation and photo-thermal therapy. *Biomaterials* **2011**, *32*, 9796–9809. [CrossRef] [PubMed]
39. Bhunia, S.K.; Saha, A.; Maity, A.R.; Ray, S.C.; Jana, N.R. Carbon nanoparticle-based fluorescent bioimaging probes. *Sci. Rep.* **2013**, *3*, 1473. [CrossRef] [PubMed]
40. Zu, X.; Yan, R.; Robbins, S.; Krishack, P.A.; Liao, D.F.; Cao, D. Reduced 293t cell susceptibility to acrolein due to aldose reductase-like-1 protein expression. *Toxicol. Sci.* **2007**, *97*, 562–568. [CrossRef] [PubMed]
41. Liu, C.J.; Zhang, P.; Tian, F.; Li, W.C.; Li, F.; Liu, W.G. One-step synthesis of surface passivated carbon nanodots by microwave assisted pyrolysis for enhanced multicolor photoluminescence and bioimaging. *J. Mater. Chem.* **2011**, *21*, 13163–13167. [CrossRef]
42. Wang, H.Q.H.; Yao, W. Melanoidins produced by the maillard reaction: Structure and biological activity. *Food Chem.* **2011**, *128*, 573–584. [CrossRef]
43. Lee, M.Y.; Lee, C.; Jung, H.S.; Jeon, M.; Kim, K.S.; Yun, S.H.; Kim, C.; Hahn, S.K. Biodegradable photonic melanoidin for theranostic applications. *ACS Nano* **2016**, *10*, 822–831. [CrossRef] [PubMed]
44. Koo, J.; Jeon, M.; Oh, Y.; Kang, H.W.; Kim, J.; Kim, C.; Oh, J. In vivo non-ionizing photoacoustic mapping of sentinel lymph nodes and bladders with icg-enhanced carbon nanotubes. *Phys. Med. Biol.* **2012**, *57*, 7853–7862. [CrossRef] [PubMed]
45. Cao, L.; Wang, X.; Meziani, M.J.; Lu, F.; Wang, H.; Luo, P.G.; Lin, Y.; Harruff, B.A.; Veca, L.M.; Murray, D.; et al. Carbon dots for multiphoton bioimaging. *J. Am. Chem. Soc.* **2007**, *129*, 11318–11319. [CrossRef] [PubMed]
46. Li, W.; Zhang, Z.; Kong, B.; Feng, S.; Wang, J.; Wang, L.; Yang, J.; Zhang, F.; Wu, P.; Zhao, D. Simple and green synthesis of nitrogen-doped photoluminescent carbonaceous nanospheres for bioimaging. *Angew. Chem. Int. Ed.* **2013**, *52*, 8151–8155. [CrossRef] [PubMed]
47. Qu, S.; Wang, X.; Lu, Q.; Liu, X.; Wang, L. A biocompatible fluorescent ink based on water-soluble luminescent carbon nanodots. *Angew. Chem. Int. Ed.* **2012**, *51*, 12215–12218. [CrossRef] [PubMed]
48. Lee, C.; Kwon, W.; Beack, S.; Lee, D.; Park, Y.; Kim, H.; Hahn, S.K.; Rhee, S.W.; Kim, C. Biodegradable nitrogen-doped carbon nanodots for non-invasive photoacoustic imaging and photothermal therapy. *Theranostics* **2016**, *6*, 2196–2208. [CrossRef] [PubMed]
49. Mieszawska, A.J.; Mulder, W.J.; Fayad, Z.A.; Cormode, D.P. Multifunctional gold nanoparticles for diagnosis and therapy of disease. *Mol. Pharm.* **2013**, *10*, 831–847. [CrossRef] [PubMed]
50. Thakor, A.S.; Jokerst, J.; Zavaleta, C.; Massoud, T.F.; Gambhir, S.S. Gold nanoparticles: A revival in precious metal administration to patients. *Nano Lett.* **2011**, *11*, 4029–4036. [CrossRef] [PubMed]
51. Naha, P.C.; Chhour, P.; Cormode, D.P. Systematic in vitro toxicological screening of gold nanoparticles designed for nanomedicine applications. *Toxicol. In Vitro* **2015**, *29*, 1445–1453. [CrossRef] [PubMed]
52. Li, W.; Chen, X. Gold nanoparticles for photoacoustic imaging. *Nanomedicine* **2015**, *10*, 299–320. [CrossRef] [PubMed]
53. Jing, L.; Liang, X.; Deng, Z.; Feng, S.; Li, X.; Huang, M.; Li, C.; Dai, Z. Prussian blue coated gold nanoparticles for simultaneous photoacoustic/ct bimodal imaging and photothermal ablation of cancer. *Biomaterials* **2014**, *35*, 5814–5821. [CrossRef] [PubMed]
54. Yoon, S.J.; Mallidi, S.; Tam, J.M.; Tam, J.O.; Murthy, A.; Johnston, K.P.; Sokolov, K.V.; Emelianov, S.Y. Utility of biodegradable plasmonic nanoclusters in photoacoustic imaging. *Opt. Lett.* **2010**, *35*, 3751–3753. [CrossRef] [PubMed]
55. Choi, H.S.; Liu, W.; Misra, P.; Tanaka, E.; Zimmer, J.P.; Itty Ipe, B.; Bawendi, M.G.; Frangioni, J.V. Renal clearance of quantum dots. *Nat. Biotechnol.* **2007**, *25*, 1165–1170. [CrossRef] [PubMed]
56. Tam, J.M.; Tam, J.O.; Murthy, A.; Ingram, D.R.; Ma, L.L.; Travis, K.; Johnston, K.P.; Sokolov, K.V. Controlled assembly of biodegradable plasmonic nanoclusters for near-infrared imaging and therapeutic applications. *ACS Nano* **2010**, *4*, 2178–2184. [CrossRef] [PubMed]
57. Weber, J.; Beard, P.C.; Bohndiek, S.E. Contrast agents for molecular photoacoustic imaging. *Nat. Methods* **2016**, *13*, 639–650. [CrossRef] [PubMed]

58. Gujrati, V.; Mishra, A.; Ntziachristos, V. Molecular imaging probes for multi-spectral optoacoustic tomography. *Chem. Commun.* **2017**, *53*, 4653–4672. [CrossRef] [PubMed]
59. Kim, J.; Park, S.; Lee, C.; Kim, J.Y.; Kim, C. Organic nanostructures for photoacoustic imaging. *ChemNanoMat* **2016**, *2*, 156–166. [CrossRef]
60. Huang, X.; Song, J.; Yung, B.C.; Huang, X.; Xiong, Y.; Chen, X. Ratiometric optical nanoprobes enable accurate molecular detection and imaging. *Chem. Soc. Rev.* **2018**, *47*, 2873–2920. [CrossRef] [PubMed]
61. Nguyen, D.N.; Yoon, H. Recent advances in nanostructured conducting polymers: From synthesis to practical applications. *Polymers* **2016**, *8*, 118. [CrossRef]
62. Park, S.J.; Park, C.S.; Yoon, H. Chemo-electrical gas sensors based on conducting polymer hybrids. *Polymers* **2017**, *9*, 155. [CrossRef]
63. Miao, Q.; Pu, K. Emerging designs of activatable photoacoustic probes for molecular imaging. *Bioconjugate Chem.* **2016**, *27*, 2808–2823. [CrossRef] [PubMed]
64. Wang, S.; Lin, J.; Wang, T.; Chen, X.; Huang, P. Recent advances in photoacoustic imaging for deep-tissue biomedical applications. *Theranostics* **2016**, *6*, 2394–2413. [CrossRef] [PubMed]
65. Jokerst, J.V.; Gambhir, S.S. Molecular imaging with theranostic nanoparticles. *Acc. Chem. Res.* **2011**, *44*, 1050–1060. [CrossRef] [PubMed]
66. Li, J.; Rao, J.; Pu, K. Recent progress on semiconducting polymer nanoparticles for molecular imaging and cancer phototherapy. *Biomaterials* **2018**, *155*, 217–235. [CrossRef] [PubMed]
67. Li, K.; Liu, B. Polymer-encapsulated organic nanoparticles for fluorescence and photoacoustic imaging. *Chem. Soc. Rev.* **2014**, *43*, 6570–6597. [CrossRef] [PubMed]
68. Li, J.; Cheng, F.; Huang, H.; Li, L.; Zhu, J.J. Nanomaterial-based activatable imaging probes: From design to biological applications. *Chem. Soc. Rev.* **2015**, *44*, 7855–7880. [CrossRef] [PubMed]
69. Lee, K.M.; Kim, K.H.; Yoon, H.; Kim, H. Chemical design of functional polymer structures for biosensors: From nanoscale to macroscale. *Polymers* **2018**, *10*, 551. [CrossRef]
70. Kim, H.; Kim, Y.; Chang, J.Y. Polymers for luminescent sensing applications. *Macromol. Chem. Phys.* **2014**, *215*, 1274–1285. [CrossRef]
71. Song, J.; Huang, P.; Duan, H.; Chen, X. Plasmonic vesicles of amphiphilic nanocrystals: Optically active multifunctional platform for cancer diagnosis and therapy. *Acc. Chem. Res.* **2015**, *48*, 2506–2515. [CrossRef] [PubMed]
72. Yoon, H. Current trends in sensors based on conducting polymer nanomaterials. *Nanomaterials* **2013**, *3*, 524–549. [CrossRef] [PubMed]
73. Park, S.J.; Kwon, O.S.; Lee, J.E.; Jang, J.; Yoon, H. Conducting polymer-based nanohybrid transducers: A potential route to high sensitivity and selectivity sensors. *Sensors* **2014**, *14*, 3604–3630. [CrossRef] [PubMed]
74. Lee, K.M.; Kim, H.J.; Jung, D.; Oh, Y.; Lee, H.; Hang, C.; Chang, J.Y.; Kim, H. Rapid accessible fabrication and engineering of bilayered hydrogels: Revisiting the cross-linking effect on superabsorbent poly(acrylic acid). *ACS Omega* **2018**, *3*, 3096–3103. [CrossRef]
75. Lee, K.M.; Oh, Y.; Chang, J.Y.; Kim, H. Facile fluorescent labeling of a polyacrylamide-based hydrogel film via radical initiation enables selective and reversible detection of Al^{3+}. *J. Mater. Chem. B* **2018**, *6*, 1244–1250. [CrossRef]
76. Jokerst, J.V.; Van de Sompel, D.; Bohndiek, S.E.; Gambhir, S.S. Cellulose nanoparticles are a biodegradable photoacoustic contrast agent for use in living mice. *Photoacoustics* **2014**, *2*, 119–127. [CrossRef] [PubMed]
77. Wang, Y.; Strohm, E.M.; Sun, Y.; Wang, Z.; Zheng, Y.; Wang, Z.; Kolios, M.C. Biodegradable polymeric nanoparticles containing gold nanoparticles and paclitaxel for cancer imaging and drug delivery using photoacoustic methods. *Biomed. Opt. Express* **2016**, *7*, 4125–4138. [CrossRef] [PubMed]
78. Kong, K.V.; Liao, L.D.; Goh, D.; Thakor, N.V.; Olivo, M. Novel biodegradable polymer tethered platinum (ii) for photoacoustic imaging. *J. Nanomed. Nanotechnol.* **2014**, *5*, 223.
79. Lyu, Y.; Zeng, J.; Jiang, Y.; Zhen, X.; Wang, T.; Qiu, S.; Lou, X.; Gao, M.; Pu, K. Enhancing both biodegradability and efficacy of semiconducting polymer nanoparticles for photoacoustic imaging and photothermal therapy. *ACS Nano* **2018**, *12*, 1801–1810. [CrossRef] [PubMed]
80. Kim, H.; Mohapatra, H.; Phillips, S.T. Rapid, On-Command Debonding of Stimuli-Responsive Cross-Linked Adhesives by Continuous, Sequential Quinone Methide Elimination Reactions. *Angew. Chem. Int. Ed.* **2015**, *54*, 13063–13067. [CrossRef] [PubMed]

81. Baker, M.S.; Kim, H.; Olah, M.G.; Lewis, G.G.; Phillips, S.T. Depolymerizable Poly(benzyl ether)-Based Materials for Selective Room Temperature Recycling. *Green Chem.* **2015**, *17*, 4541–4545. [CrossRef]
82. Yeung, K.; Kim, H.; Mohapatra, H.; Phillips, S.T. Surface-Accessible Detection Units in Self-Immolative Polymers Enable Translation of Selective Molecular Detection Events into Amplified Responses in Macroscopic, Solid-State Plastics. *J. Am. Chem. Soc.* **2015**, *137*, 5324–5327. [CrossRef] [PubMed]
83. Kim, H.; Ryu, J.H.; Kim, H.K.; Chang, J.Y. A versatile platform for lanthanide(III)-containing organogelators: fabrication of the Er(III)-incorporated polymer nanocomposite from an organogel template. *New J. Chem.* **2017**, *41*, 12366–12370. [CrossRef]
84. Kim, H.; Chang, J.Y. Reversible Thermochromic Polymer Film Embedded with Fluorescent Organogel Nanofibers. *Langmuir* **2014**, *30*, 13673–13679. [CrossRef] [PubMed]
85. Kim, H.; Chang, J.Y. White light emission from a mixed organogel of lanthanide(III)-containing organogelators. *RSC Adv.* **2013**, *3*, 1774–1780. [CrossRef]
86. Kim, H.; Chang, J.Y. Synthesis of a film-forming europium(III) complex and its organogelation and photoluminescent properties. *Soft Matter* **2011**, *7*, 7952–7955. [CrossRef]